

Journal of Biomedical Optics

SPIEDigitalLibrary.org/jbo

Measurement of absolute cell volume, osmotic membrane water permeability, and refractive index of transmembrane water and solute flux by digital holographic microscopy

Daniel Boss
Jonas Kühn
Pascal Jourdain
Christian Depeursinge
Pierre J. Magistretti
Pierre Marquet

Measurement of absolute cell volume, osmotic membrane water permeability, and refractive index of transmembrane water and solute flux by digital holographic microscopy

Daniel Boss,^a Jonas Kühn,^b Pascal Jourdain,^a Christian Depeursinge,^c Pierre J. Magistretti,^a and Pierre Marquet^a

^aEcole Polytechnique Fédérale de Lausanne, Laboratory of Neuroenergetics and Cellular Dynamics, Lausanne, Switzerland

^bCentre de Neurosciences Psychiatriques, Département de Psychiatrie DP-CHUV, Prilly-Lausanne, Switzerland

^cEcole Polytechnique Fédérale de Lausanne, Microvision and Microdiagnostics Group, Lausanne, Switzerland

Abstract. A dual-wavelength digital holographic microscope to measure absolute volume of living cells is proposed. The optical setup allows us to reconstruct two quantitative phase contrast images at two different wavelengths from a single hologram acquisition. When adding the absorbing dye fast green FCF as a dispersive agent to the extracellular medium, cellular thickness can be univocally determined in the full field of view. In addition to the absolute cell volume, the method can be applied to derive important biophysical parameters of living cells including osmotic membrane water permeability coefficient and the integral intracellular refractive index (RI). Further, the RI of transmembrane flux can be determined giving an indication about the nature of transported solutes. The proposed method is applied to cultured human embryonic kidney cells, Chinese hamster ovary cells, human red blood cells, mouse cortical astrocytes, and neurons. © 2013 Society of Photo-Optical Instrumentation Engineers (SPIE) [DOI: 10.1117/1.JBO.18.3.036007]

Keywords: digital holographic microscopy; absolute cell volume; intracellular refractive index; osmotic membrane water permeability; dry mass concentration; transmembrane solute transport.

Paper 12662 received Oct. 4, 2012; revised manuscript received Dec. 9, 2012; accepted for publication Jan. 2, 2013; published online Mar. 13, 2013.

1 Introduction

Membranes of animal cells are highly permeable to water; movement of water across membranes is therefore dictated in large part by osmotic pressure gradients.¹ Any imbalance in intracellular and extracellular osmolarity is paralleled by water movements across cell membranes affecting cell volume along with the concentration of intracellular compounds.² However, even at constant extracellular osmolarity, volume constancy of any mammalian cell is permanently challenged by the normal activity of the cells.^{1,3} Thus, the maintenance of a constant volume is critical for cell homeostasis and requires the continued operation of cell volume regulatory mechanisms.^{1,4} Water crosses membrane through several routes (simple diffusion through the lipid bilayer, transmembrane proteins, specialized water channels, aquaporins, AQP, etc.). Membrane water permeability P_f represents therefore an index which can provide information about the different mechanisms involved in the transmembrane water movements. Consequently, a technique that provides real time quantitative measurements of both cell volume and osmotic water permeability P_f while retaining the cell functionality would represent an efficient time-resolved tool to investigate the complex and multiple mechanisms underlying cell volume regulation.

Absolute cell volume measurements have been successfully achieved by confocal fluorescence imaging,⁵ staining of membrane surfaces with fluorescent beads,⁶ transmission-

through-dye based estimation of cellular thickness.^{7,8} Such techniques are either limited by their low temporal resolution as they involve optical scanning^{5,6} or are only applicable for cells that show no light absorption.^{7,8} Only relative cell volume variations can be assessed by techniques that measure changes of intracellular fluophore concentration,^{9,10} or volume dependent fluorescence quenching.¹¹ A drawback of these techniques is that they allow only the measurement of variations of fluorescently labeled compartments of the cell volume. Other techniques that are not based on light microscopy and that do not allow the assessment of volume variations at a single cell level have been proposed. Cell content dilution has been assessed by measuring equilibrium concentration of radio labeled molecules¹² and cell volume variations could be correlated with electrical resistance changes of the cell chamber.¹³

The osmotic membrane water permeability P_f is in turn usually determined by measuring the relative cell volume time course in response to an osmotic gradient applied between intracellular and extracellular compartments.^{10,11,14,15} Indeed, techniques providing such relative cell volume measurements offer the advantage of a high temporal resolution combined with low computational cost and low data storage capacity requirements.

Our approach is based on digital holographic microscopy which has demonstrated its capacity to efficiently image living cells by accurately recording the phase retardation of a light wave when transmitted through a transparent specimen.^{16–20} Practically, this phase retardation contrast, proportional to the thickness of the observed specimen, is a result of the difference

Address all correspondence to: Daniel Boss, Ecole Polytechnique Fédérale de Lausanne, Laboratory of Neuroenergetics and Cellular Dynamics, Lausanne, Switzerland. Tel: +41.21.693.17.24; E-mail: daniel.boss@a3.epfl.ch

in refractive indices between the specimen and the surrounding medium. Consequently, quantitative phase signal provides information about both cell morphology and intracellular content related to the refractive index. Although the quantitative phase signal depends on both, cell volume and integral refractive index (RI), conventional quantitative phase microscopy (QPM) techniques do not allow to measure these two parameters separately and consequently, cell volume cannot be inferred from the quantitative phase information. Nevertheless, attempts to determine separately cell volume and intracellular RI from the quantitative phase signal have been made by an experimental phase decoupling procedure,²¹ by placing cells into a known confining geometry²² or by deducing a cell radius of spherical cells in suspension.²³ However, all of these approaches present drawbacks. In the first case of experimental phase decoupling,²¹ the measurement cannot be performed in a continuous fashion to monitor dynamic volume variations, confined geometry approaches²² can only be performed on a few cells which are placed in the confinement and whose cell height matches the dimension of the confinement. Finally, cell radius determination²³ restrict measurement to spherical cells in suspension. A promising method to measure cell volume and intracellular RI, which exploits the dye-enhanced dispersion of the extracellular medium, has been proposed in a proof of principle paper by Rappaz et al.²⁴ Here, based on this dye-enhanced dispersion approach, we have developed a single shot dual-wavelength digital holographic microscope (DHM) strategy as an efficient tool to accurately measure the dynamics of absolute cell volume and intracellular RI. As described by Kühn et al.,²⁵ the proposed transmission dual-wavelength DHM setup allows us to reconstruct two quantitative phase images at different wavelengths from a single hologram acquisition. Practically, dispersion enhancement of the extracellular medium is obtained by adding the absorbing fast green FCF dye to the perfusion solution.

We applied this approach to the study of water permeability coefficient P_f based on monitoring of absolute cell volume in a variety of cell types, including red blood cells (RBC), cultured Chinese hamster ovary (CHO), and human embryonic kidney (HEK) cell lines as well as primary cultures of neurons and astrocytes. We further investigated the relation between intracellular integral RI and cell volume and could show how dual-wavelength DHM combined with dye-enhanced dispersion of the extracellular medium can be applied to measure the RI of transmembrane fluxes.

2 Materials and Methods

2.1 Cell Culture

Wild-type CHO cells and HEK 293 cells were cultured at 37°C in 5% CO₂ and maintained in a minimum essential medium containing 7% fetal bovine serum and 0.5% antibiotics (50 IU/ml penicillin and 50 µg/ml streptomycin). Primary astrocyte cultures were prepared from neocortical tissue of newborn mice as described in Ref. 26. Briefly, cells were grown to confluence on polyornithine coated glass cover slips in Dulbecco's modified Eagle's medium (DMEM/ D7777 sigma) containing antibiotics (100 IU/ml penicillin and 100 µg/ml) and 10% fetal calf serum (FCS). Cells were incubated at 37°C in 5% CO₂ and the medium was changed twice a week. After two weeks, the medium was replaced by DMEM containing 10% FCS and 250 µM dibutyl cAMP to induce differentiation. Cells were used for experiments three to five weeks after dissection.

Neuronal cell cultures were prepared as described in Ref. 27. Briefly, primary cultures of cortical neurons were prepared from mice embryos and transferred into dishes containing glial cell monolayers. Neurons were maintained in supplemented Neurobasal medium at 37°C in 5% CO₂ and were used for experiments after 21 to 35 days. For the RBC preparation, 100 to 150 µl of blood was drawn from a healthy laboratory person by fingerpick, collected and diluted at a ratio of 1:10 (v/v) in cold HEPES buffer (15 mM HEPES pH 7.4, 130 mM NaCl, 5.4 mM KCl, 10 mM D-glucose, 1 mM CaCl₂, 0.5 mM MgCl₂ and 1 mg/ml bovine serum albumin). Blood cells were sedimented at 200 g, 4°C for 10 min and buffy coat was gently removed. RBCs were washed twice in HEPES buffer (1000 g×) 2 min at 4°C). About 8 µl of the RBC suspension was added onto a polyornithine coated cover slip and incubated at 37°C for 1/2 h prior to mounting of the cover slip onto the cell chamber.

2.2 Perfusion Medium

The standard perfusion medium contains (in mM): NaCl 140, KCl 3, D-glucose, 5, HEPES 10, CaCl₂ 3, and mM MgCl₂ 2. The pH is set to 7.3 and all experiments are carried out at room temperature. The dispersion enhancement is achieved by adding 20 mM fast green FCF (Sigma) to the standard medium. Additionally, water is added to preserve an osmolarity of the perfusion solution of 300 mOsm. Osmolarities are measured with a freezing point depression osmometer (Roebing osmometer 13DR) and refractive indices of the extracellular medium are measured with an Abbe-Refractometer (Nade 2WJ) in reflection mode. The absorption spectrum shown in Fig. 1 is derived from an absorption spectrum of a solution with a lower dye concentration, measured with a Tecan Safire plate reader.

2.3 Dual-Wavelength-DHM Setup

Figure 2 shows the schematic of the dual-wavelength DHM setup. It consists of two basic DHM Mach-Zehnder interferometers that share a common object path, but have a distinct

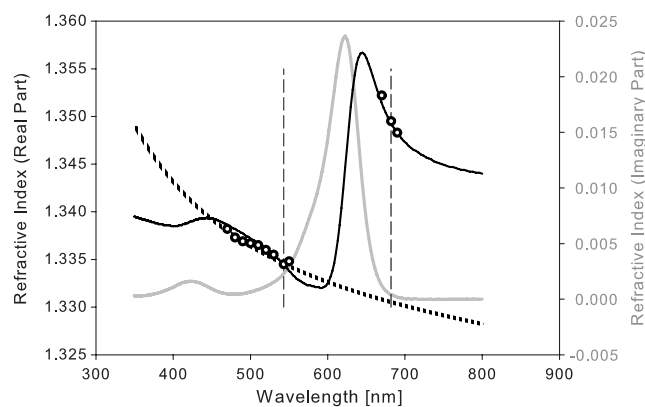


Fig. 1 Gray line: imaginary part of RI of 20 mM fast green FCF solution as a function of wavelength. The curve was derived from an absorption spectrum of a 500 µM fast green FCF solution. Black line: real part of RI of 20 mM fast green solution calculated via Kramer-Kronig relation, Black circles: real part of RI of 20 mM fast green solution measured with an Abbe-Refractometer. The value at 543 nm corresponds to the measured RI. For the other wavelengths RI dispersion of water is subtracted. Black dashed line: water RI dispersion Sellmeyer-equation at 24 taken from Ref. 28. Vertical dashed lines: recording wavelengths.

reference path. A He-Ne laser ($\lambda_1 = 543$ nm) and a laser diode ($\lambda_2 = 682$ nm) are used as light sources. Object waves are magnified by a 63x oil immersion objective (NA = 1.4) and interfere with the reference waves to form a dual-wavelength hologram recorded by a charge-coupled device camera (Basler A101f). By adjusting the off-axis angle of the two reference beams separately, one can adjust the orientation of the

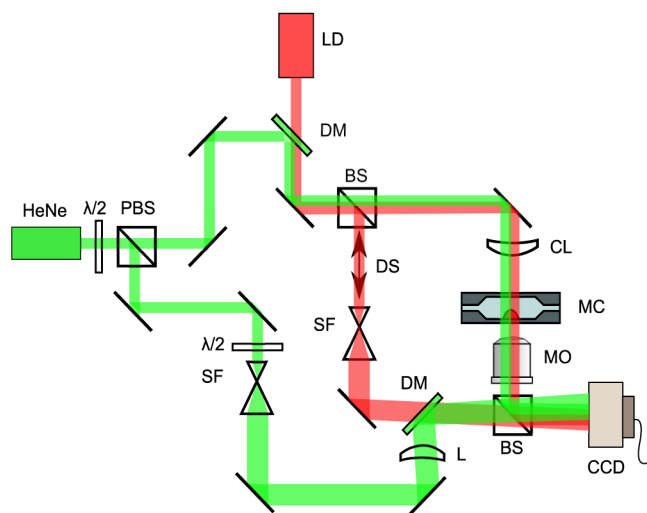


Fig. 2 Schematic representation of optical setup. LD: laser diode $\lambda = 682$ nm; HeNe: helium neon laser $\lambda = 543$ nm; DM: dichroic mirror; BS: beam splitter; PBS: polarizing beam splitter; $\lambda/2$: half wave plate; DS: delay stage; SF: spatial filter; CL: condenser lens; MC: microscopy chamber; MO: microscope objective; and CCD: charge-coupled device camera.

interference fringes to lie orthogonally to each other [see Fig. 3(a)]. The frequency content of each object wave is then filtered in the Fourier space of the hologram and phase images are reconstructed individually with the standard Fourier reconstruction algorithm in DHM.²⁹ Holograms are acquired in focus and digital propagation of electric fields is therefore omitted. For imaging, cells are mounted on a custom made flow chamber in which the height of the chamber is limited to approximately $200 \mu\text{m}$ in order to reduce light absorbance by the dye. Data were processed using MATLAB R2008a (The Mathworks, Natick, Massachusetts). In one case, a differential equation was solved by using Mathematica 7 (Wolfram Research, Champaign, Illinois). For hypothesis testing, a paired students t test is performed.

3 DHM Quantitative Phase Signal

The phase retardation φ induced by a cell can be given in terms of the cellular parameters as

$$\varphi = \frac{2\pi}{\lambda} d(n_c - n_s) \propto d\Delta n = \text{OPD}. \quad (1)$$

Here, λ denotes the wavelength, d cellular thickness, n_c integral refractive index (RI), defined as the mean cellular RI along the optical axis, n_s the refractive index of the extracellular solution, and OPD is the optical pathlength difference. Net water flux across the cell membrane causes both a swelling or shrinkage of the cell and a variation of the concentration of the intracellular components, in particular proteins, resulting in a integral RI change. However, the actual variations of both parameters cannot be determined based on a single phase measurement. Moreover, during water flux across cell membrane an increase

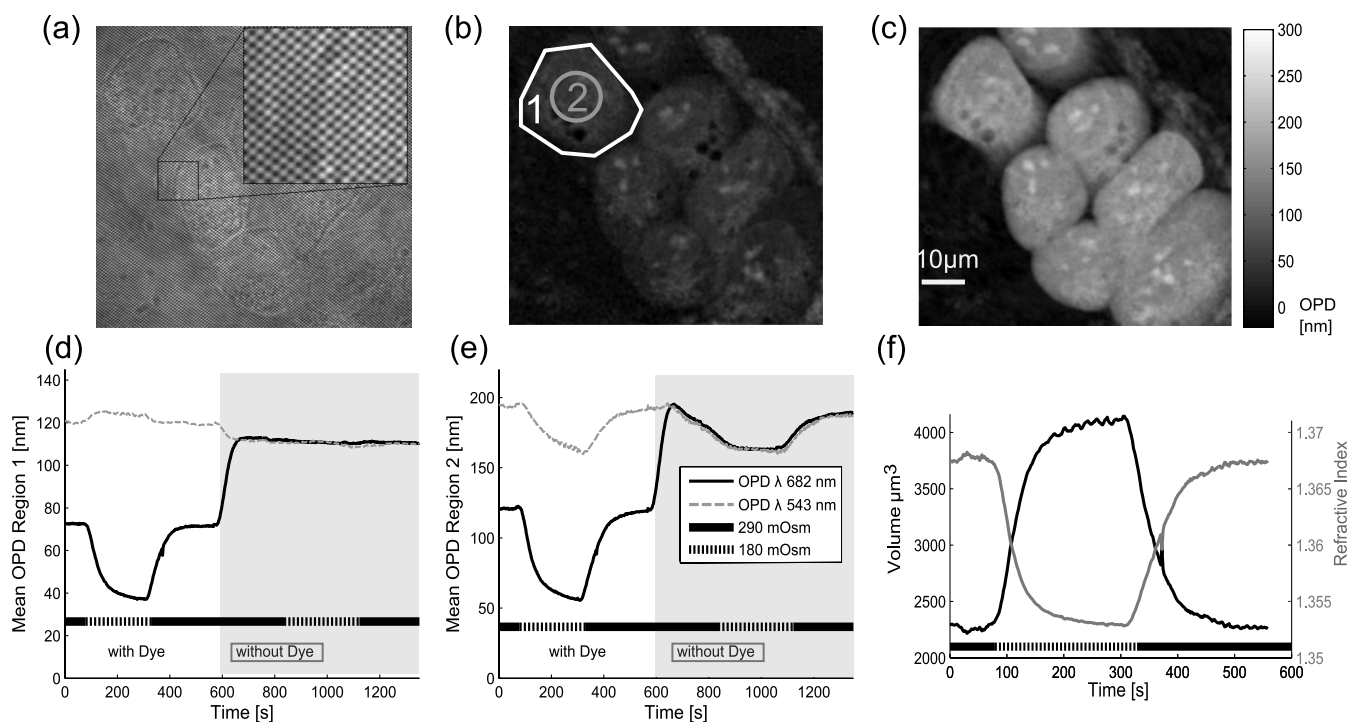


Fig. 3 (a) Dual-wavelength hologram of HEK cells with zoom on interference fringes. (b) Reconstructed OPD image at $\lambda = 682$ nm. (c) Reconstructed OPD image at $\lambda = 543$ nm. (d) Mean OPD signal of region 1 depicted in B during a hypotonic challenge in the presence or absence of fast green FCF dye 20 mM in the extracellular solution. (e) Mean OPD signal of region 2 depicted in B. (f) Cellular volume and integral RI during hypotonic challenge derived from OPD measurements shown in D.

of one parameter (e.g., d) is accompanied by a decrease of the other parameter (e.g., n_c). Therefore, when translating variations of the parameters d and n_c into phase variations φ , some part of the signal is annihilated.

3.1 Phase Decoupling Procedure

The phase ambiguity can be resolved with two consecutive phase measurements at two different wavelengths when adding a highly dispersive agent to the extracellular medium. As a dispersive agent, the absorbing dye fast green is added to the extracellular medium. Laser wavelengths are chosen on either side of the absorption peak in order to fully exploit the anomalous dispersion regime of the dye. Figure 1 shows the imaginary part of the refractive index of 20 mM fast green FCF in a physiological solution. The real part of the refractive index, which is derived from the imaginary part of the RI by the Kramer-Kronig relation, is in good agreement with measured refractive indices at different wavelengths. To derive explicit formulas for cell thickness and integral RI, we write the intracellular RI $n_c(\lambda)$ as the sum of water RI $n_{H_2O}(\lambda)$ and the contribution of intracellular dry mass (proteins, lipids, ...). As proposed by Barer et al.,³⁰ this contribution is written as the product specific refractive increment of cell dry mass α_c times the cell dry mass concentration C_c :

$$n_c(\lambda) = n_{H_2O}(\lambda) + \alpha_c C_c, \quad (2)$$

Similarly, the extracellular RI $n_s(\lambda)$ is written in terms of water RI, contribution of dye [refractive increment of dye $\alpha_{Dye}(\lambda)$ times the concentration of dye C_{Dye}] and contribution of other substances present in the extracellular solution (mean refractive index increments of ions and metabolites α_r times their concentration C_r):

$$n_s(\lambda) = n_{H_2O}(\lambda) + \alpha_{Dye}(\lambda)C_{Dye} + \alpha_r C_r. \quad (3)$$

Here, we assume that extracellular dispersion is caused by water dispersion [$n_{H_2O}(\lambda)$] and dispersion of added dye [$n_{Dye}(\lambda)$] and the wavelength dependency of intracellular RI is primarily caused by water dispersion. The wavelength dispersion of the other terms ($\alpha_c C_c, \alpha_r C_r$) are assumed to be negligible compared to dispersion of water and dye (further discussed in Sec. 4.1).

Solving for the unknown cell parameters d and $n_c(\lambda)$ by introducing the two OPD measurements $OPD_{\lambda_1}, OPD_{\lambda_2}$ leads to

$$d = \frac{OPD_{\lambda_1} - OPD_{\lambda_2}}{[\alpha_{Dye}(\lambda_2) - \alpha_{Dye}(\lambda_1)]C_{Dye}} = \frac{OPD_{\lambda_1} - OPD_{\lambda_2}}{\Delta n_{Dye}(\lambda_{2,1})}, \quad (4)$$

$$n_c(\lambda_1) = \frac{OPD_{\lambda_1} \times \Delta n_{Dye}(\lambda_{2,1})}{OPD_{\lambda_1} - OPD_{\lambda_2}} + n_s(\lambda_1).$$

The intracellular RI n_c is given for the laser wavelength $\lambda_1 = 543$ nm. All the measured intracellular RI n_c in this article refer to this wavelength. The term $\Delta n_{Dye}(\lambda_{2,1})$ denotes the RI difference at the two laser wavelengths $\lambda_{2,1}$ that is due solely to the dispersion of dye. This term is measured experimentally by subtracting the dispersion of water from the measured RI of the extracellular solution: $\Delta n_{Dye}(\lambda_{2,1}) = \Delta n_s(\lambda_{2,1}) - \Delta n_{H_2O}(\lambda_{2,1})$.

4 Results and Discussion

As a first validating experiment, we measured the volume and integral RI time course in a HEK cell during an osmotic challenge. Figure 3(b) and 3(c) shows OPD images of the swollen cells in the hypotonic extracellular solution. Figure 3(d) and 3(e) shows the mean OPD time courses of the selected regions defined in Fig. 3(b), i.e., a region integrating over an area containing the whole cell, and a region inside the perimeter of the cell. The hypotonic challenge was performed twice: first by perfusing the chamber with a hypotonic medium containing the dye, and second with a medium containing no dye. In the absence of dye, one readily sees that the intrinsic RI cell dispersion is negligible when comparing OPD differences between the two wavelengths. Also, it can be seen that there is practically no phase signal variation during an osmotic challenge when the phase signal is integrated over the entire cell surface area [see Fig. 3(d)], meaning a conservation of the cell dry mass (an indicator of the cell biomass resulting mainly from the protein content)³¹ during the osmotic shock. However, in the presence of dye in the extracellular solution the two OPD time courses are significantly different during the hypo osmotic shock. At the wavelength $\lambda_2 = 682$ nm, due to the presence of dye, the extracellular RI is considerably increased compared to the RI of the entering water. Consequently, a strongly amplified OPD variation results in response to water flux. Thus, when the dye significantly modifies the extracellular RI, the OPD signal during an osmotic challenge is not only sensitive to variations of the dry mass spatial distribution but also to the transmembrane water flux. Coherently, at the wavelength $\lambda = 543$ nm, the minute OPD increase [Fig. 3(d), gray dashed curve] results from a slightly lowered extracellular RI due to the anomalous dispersion of the fast green FCF dye. Finally, the derived volume and mean integral RI time course, as shown in Fig. 3(f), can be determined.

4.1 Precision and Accuracy of the Measurements

The measurement precision of the cell parameters n_c and d depends strongly on the precision of the OPD signals. In the presence of noise in the measured OPD signal, evaluated as the temporal standard deviation α of consecutive OPD measurements in time, i.e., $\text{std}[OPD_{\lambda_1,2}(t)] = \alpha_{1,2}$, the standard deviation on the measured cell parameters d and n_c is

$$\text{std}(d) = \sqrt{\frac{\alpha_1^2 + \alpha_2^2}{[\Delta n_{Dye}(\lambda_{2,1})]^2}},$$

$$\text{std}(n_c) \approx \left[\sqrt{\frac{(\beta_2 \alpha_2)^2 + (\beta_1 \alpha_2)^2}{d}} \right], \quad (5)$$

$$\beta_i = \frac{2(n_c - n_{s\lambda i})}{\Delta n_{Dye}(\lambda_{2,1})}.$$

The hypothesis leading to these expressions is that the noise on the two OPD signals is uncorrelated and independent of the cellular parameters. The expression of the standard deviation of n_c was derived from a second order Taylor expansion of the function $n_c(OPD_{\lambda_1}, OPD_{\lambda_2})$.

The expected standard deviation on the thickness measurement is then inversely proportional to the difference in RI of extracellular solution at the recording wavelengths $\Delta n_{Dye}(\lambda_{2,1})$. This value depends linearly on the concentration of dye added

to the medium. Therefore, a compromise has to be found between the desired precision and the perturbation of the intra- and extracellular ionic concentrations induced by the dye. In contrast, the precision of the measured value n_c depends on the cell parameters; the expected standard deviation is inversely proportional to the cell thickness and depends on the intracellular RI itself. Theoretically, the best signal-to-noise ratio (SNR) could be expected for an intracellular RI of $n_c = (n_{s\lambda 2} + n_{s\lambda 1})/2 \approx 1.34$ in the case of equal noise amplitude on both OPD signals. The typical intracellular RI n_c for most cells is, however, situated around 1.36 to 1.4 and consequently the SNR value for the intracellular RI n_c is lower than what could be theoretically obtained. The measurement precision was assessed in CHO cells by evaluating the standard deviation of the cell parameters during 40 s of acquisition. Spatially averaged OPD signals on the cell body showed a temporal standard deviation of $\alpha_{1,2} \approx 0.4$ nm, leading to a measurement precision on the mean cellular thickness of $\text{std}(d) \approx 34$ and 69 nm for dye concentrations of 20 and 10 mM, respectively. Figure 4 shows that the experimental measurement precision on the mean integral RI of three different CHO cells correlates, as predicted, with the respective height. For a cell thickness of $h \approx 10 \mu\text{m}$ a precision of $\text{std}(n_c) \approx 5 \times 10^{-5}$ is achieved. Due to coherent noise, shot-noise, and noise added in the digital reconstruction process the measurement precision on a single-pixel level is about an order of magnitude lower in comparison to measurements averaged on the cell body. Apart from noise on the OPD signal, the accuracy of the measurements of the cell parameters can be influenced by some additional sources of error, including the accuracy of the determination of the extracellular RI $n_s(\lambda_{1,2})$, and the subtraction of optical path length reference values corresponding to background regions where there is no biological material. Occasionally, in dense cell cultures such background regions cannot be delimited easily. A small error in the measurement of the cell parameters is also introduced by the assumption that refractive increments of cell dry mass (proteins, lipids) α_c is wavelength independent. Dispersion of specific refractive increments of some purified proteins like bovine serum albumin has been measured in the past³² and modeled according to Eq. (6).

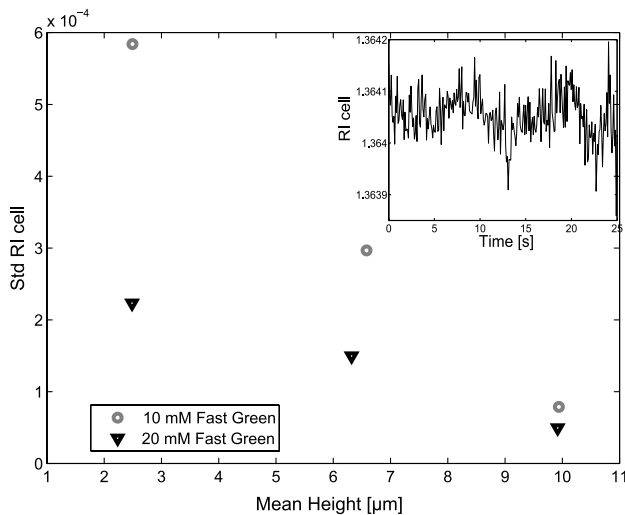


Fig. 4 Measurement precision of intracellular RI as a function of height of CHO cells. Temporal standard deviations were calculated from time series measurements as shown in the inset.

$$\alpha_c(\lambda) = \alpha_c(578 \text{ nm}) \times \left(0.940 + \frac{20000 \text{ nm}}{\lambda^2} \right). \quad (6)$$

For a typical intracellular RI of ≈ 1.38 , such a refractive increment dispersion would yield a difference in RI at the two measuring wavelength of $\approx 1 \times 10^{-3}$ or, equivalently, OPD differences of ≈ 5 nm for an average cell thickness of $5 \mu\text{m}$. Although this error is small, it is still bigger than the measurement precision. However, when performing control experiments without dye in the perfusion medium no significant differences between OPD measurements could be detected ($\Delta\text{OPD} = 0.56 \pm 3.6$, $n = 36$ CHO cells, $p = 0.23$). Thus, refractive increment dispersion of intracellular dry mass is presumably lower than dispersion of specific proteins, and the resulting error in accuracy is in the order of the measurement precision.

4.2 Osmotic Membrane Water Permeability Measurement

The osmotic membrane water permeability P_f of a semi-permeable membrane determines the water volume flux per unit of time per unit of membrane surface for a given applied osmotic gradient.^{14,33} For a closed cell membrane, it is measured according to Eq. (7),

$$P_f = \frac{1}{v_w A_0 \Delta\Pi_0} \left(\frac{\partial V}{\partial t} \right)_0 = \frac{\Delta V}{\tau v_w A_0 \Delta\Pi_0}, \quad (7)$$

where $\Delta\Pi_0$ is the initially applied osmotic gradient between intra- and extracellular compartments, v_w the partial molar volume of water, A_0 the cell surface area, and $(\partial V/\partial t)_0$ the initial cell volume change rate. This last value is practically determined by fitting an exponential decay function, parameterized as $V(t) = V_0 + \Delta V \times \{1 - \exp[-(t/\tau)]\}$, to the volume time course, from which the fitted values of τ and ΔV are determined. The cell surface area A_0 is evaluated based on two assumptions. First, the surface area is evaluated in the swollen state. In fact, because cell membranes can only stretch their surface area by approximately 2% to 3% before undergoing lysis,³⁴ it is presumably the case that the apparent surface expansion during swelling is mainly due to an unfolding of the membrane. Consequently, an evaluation of the surface area in the swollen state minimizes an underestimation of the actual surface area, i.e., the area of the folded membrane surface through which water can pass during the osmotic challenge. Second, we assume that water flow through the cell membrane that attaches to the coverslip is strongly reduced and does not substantially contribute to the water permeability of the cell. Thus, we neglect the surface in contact with the coverslip and calculate the surface area A_0 by interpolating the cell thickness by a triangular mesh for which the surface area is evaluated [see Fig. 5(b)].

The membrane water permeability was measured according to Eq. (7) in CHO cells ($n = 46$), HEK cells ($n = 14$), neurons ($n = 11$), astrocytes ($n = 19$), and red blood cells (RBCs) ($n = 22$) when applying a hypo osmotic challenge. Table 1 shows the retrieved experimental data from which an average P_f value of 0.00165 cm/s for CHO cells, 0.00304 cm/s for HEK cells, 0.00469 cm/s for neurons, 0.00764 cm/s for astrocytes, and 0.0052 cm/s for RBCs was calculated [see Fig. 5(d)].

The high membrane water permeability of human RBCs is mainly determined by the endogenously expressed water

channel AQP1.^{35,36} In the past, approximately 4-fold higher values for the osmotic water permeability coefficient in human RBCs have been reported.³⁵ We cannot exclude that this discrepancy with our measurements might be due to a limited solution exchange in the cell chamber (≈ 1 s) that doesn't yield a sufficiently fast step response in extracellular osmolarity compared to the measured time constant τ , leading to an underestimation of the P_f value for the RBC. However, the RBC provides an example where the water transport mechanism can easily be altered by pharmacological inhibition of AQP1 with mercury chloride HgCl₂, a potent, rapid inhibitor of AQP1.³⁵ After a first hypo osmotic challenge on the RBC preparation, the cell chamber is perfused for 100 s with a solution containing 200 μ M HgCl₂ before the second hypo osmotic challenge is applied. Figure 5(a) shows the mean volume time course of $n = 10$ RBCs in response to the osmotic challenge with or without addition of HgCl₂ to the perfusion medium. A slower cell volume equilibration is observed when inhibiting AQP1 with HgCl₂, both when decreasing and re-increasing the osmolarity of the medium. The permeability coefficient P_f was reduced in all cells, in average by a factor of 4.333 ± 2.69 to a value of 1.5 ± 1.2 cm/s ($p < 0.001$).

In wild-type CHO cells a P_f value of 0.0012 cm/s has been reported by Farinas et al.,³⁷ which is in good agreement with our measurements. Comparable results on HEK cells have been shown by Gao et al.³⁸ In our measurements, the P_f coefficient in astrocytes was about 5-fold higher than in wild-type CHO cells. The membrane water permeability in astrocytes has so far been measured with fluorescence based methods and reported values range from 0.05 to 0.0008 cm/s.^{10,11,39} The high water permeability in astrocytes is usually attributed to the endogenously expressed water channel aquaporin AQP4 (Refs. 10, 40, and 41) and it has been shown that astrocytes from AQP4 deficient mice show a 7-fold reduced osmotic water permeability.¹¹ The water permeability measured in primary cultures of neurons was about 3-fold higher than in wild-type CHO cells. Presumably, this higher water permeability cannot be attributed to aquaporin channels, as aquaporin expression in the brain parenchyma is primarily observed in astrocytes and in specific neuronal subtypes such as brain stem catecholaminergic neurons.^{41,42} A possible explanation of the increased water permeability in neurons compared to wildtype CHO cells could be an increased expression of specific solute transporters that exhibit an intrinsic water permeability.⁴³

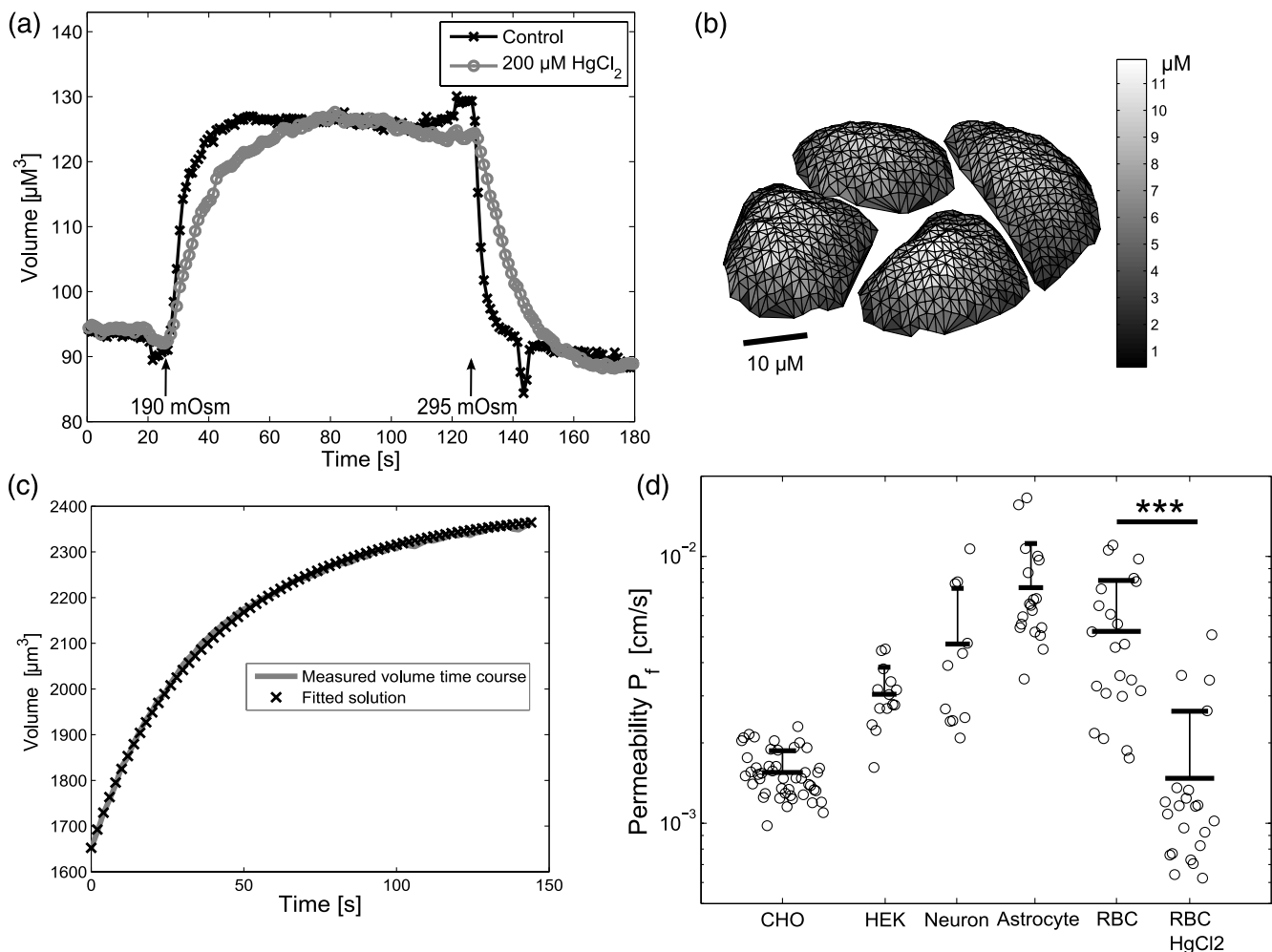


Fig. 5 (a) Mean volume timecourse of $n = 10$ RBCs during a hypoosmotic challenge (black line). A second challenge was performed on the same cells when 200 μM HgCl₂ was present in the perfusion medium (gray line). (b) Height profile image of CHO cells interpolated by a triangular mesh. Cell surface area is evaluated on mesh. (c) Mean volume time course of $n = 46$ CHO cells during an osmotic challenge (gray line) and fitted solution to the differential equation governing the volume time course (black cross). (d) Membrane water permeability coefficient P_f of $n = 46$ CHO cells, $n = 14$ HEK cells, $n = 11$ neurons, $n = 19$ astrocytes, and $n = 22$ RBCs with or without 200 μM HgCl₂ present in the medium. P_f is on a logarithmic scale.

Table 1 Osmotic challenge: measured parameters in different cell types.

	V_0 (μm^3)	ΔV (μm^3)	$(\Delta V + V_0)/V_0$	Π_i/Π_o	A_0 (μm^2)	τ (s)	P_f (10^{-3} cm/s)
CHO	1660 ± 669	718 ± 294	1.4341 ± 0.065	1.452	747 ± 340	33.71 ± 5.6	1.65 ± 0.318
HEK	1996 ± 562	1437 ± 377	1.739 ± 0.16	1.667	676 ± 153	34.6 ± 10.9	3.04 ± 0.87
Neuron	1671 ± 1116	609 ± 429	1.376 ± 0.09	1.452	475 ± 226	17.8 ± 8.42	4.69 ± 2.89
Astrocyte	861 ± 324	347 ± 132	1.463 ± 0.319	1.452	475 ± 137	6.44 ± 2.78	7.64 ± 3.54
RBC	95 ± 48	35 ± 11	1.457 ± 0.277	1.553	129 ± 44	3.62 ± 2.05	5.2 ± 2.9
RBC/HgCl ₂	101 ± 49	33 ± 14	1.41 ± 0.30	1.553	135 ± 45	11.17 ± 4.8	1.5 ± 1.2

In contrast to our results, a low water permeability in freshly isolated CA1 pyramidal neurons⁴⁴ and in cortical pyramidal cells in slice preparations⁴⁵ has been reported. Surprisingly, often an absence of neuronal swelling or shrinkage in response to osmotic challenges was observed.⁴⁵

In all the measurements, the ratio of final volume to initial volume $(\Delta V + V_0)/V_0$ corresponds well with the respective ratio of the initial osmolarity to the hypo osmotic osmolarity Π_i/Π_o (see Table 1), suggesting that intracellular and extracellular osmolarity are rendered equal mainly through water flux across the membrane and that active processes such as regulatory volume decrease (RVD) did not strongly influence cell volume within the short measurement period. Assuming that cells behave like a perfect osmometer, the osmolarity difference across the membrane $\Delta\Pi$ can be expressed at any moment in time in terms of $V(t)$, V_0 , Π_i , and Π_o . Following Eq. (7), a differential equation that governs the volume time course $V(t)$ during an osmotic challenge can thus be derived:

$$\frac{\partial V(t)}{\partial t} = P_f v_w A_0 \Delta\Pi(t) = P_f v_w A_0 \left[\frac{V_0 \Pi_i}{V(t)} - \Pi_o \right]. \quad (8)$$

A solution to Eq. (8) is found numerically and is fitted to the mean volume time course of $n = 46$ CHO cells during a hypo osmotic challenge [see Fig. 5(c)]. Good agreement between measured and theoretically evaluated volume time course is observed when the modeled solution is fitted to the experimental data by adjusting the free parameter $P_f \times A_0$. This agreement suggests that the product of water permeability coefficient and surface area $P_f \times A_0$ can adequately be modeled as a constant term throughout the osmotic challenge. Thus, a possible unfolding of the membrane does presumably not strongly alter the effective membrane surface area available for transmembrane water movement.

4.3 Determination of Refractive Index of Transmembrane Water and Solute Flux

The RI of most solutions increases linearly with the concentration of the dissolved solute. The factor of proportionality that relates the two quantities is the specific refractive increment α . Accordingly, Barer et al.³⁰ related the intracellular RI of cells to the dry mass concentration C via a cell specific refractive increment α :

$$n_c = n_0 + \alpha C = n_0 + \alpha \frac{m}{V}. \quad (9)$$

Here, n_0 denotes the solvent RI, m the cellular dry mass, and V the cell volume. A mean value of $\alpha = 0.185$ and 0.1899 ml/g, respectively, has been reported for soluble proteins^{31,46} and the solvent RI n_0 corresponds to water RI.

An interesting application of the method is the determination of the RI of transmembrane fluxes n_f . We consider a transmembrane flux of water and solutes characterized by an RI of $n_f = n_0 + \alpha_f C_f$ beginning at $t = t_0$ that leads to an accumulation of dry mass:

$$\begin{aligned} m(t) &= m(t_0) + \int_{t_0}^t C_f \frac{\partial V(t)}{\partial t} dt \\ &= m(t_0) + C_f \times [V(t) - V_0]. \end{aligned} \quad (10)$$

Here, the solute concentration C_f of the flux is assumed to be constant in the interval $[t_0; t]$. Expressing $n_c(t)$, when taking into account the transmembrane flux, yields:

$$n_c(t) = n_0 + \frac{\alpha_f C_f \times [V(t) - V_0]}{V(t)} + \frac{\alpha m(t_0)}{V(t)}. \quad (11)$$

Substituting in Eq. (11), the initial dry mass $m(t_0)$ by using the relation in Eq. (9) and solving for the RI of the transmembrane flux $n_f = n_0 + \alpha_f C_f$ yields

$$n_f = \frac{n_c(t) \times V(t) - n_c(t_0) \times V(t_0)}{V(t) - V(t_0)}. \quad (12)$$

From Eq. (11) it also follows that the term

$$k(t) = [n_c(t) - n_0 - \alpha_f C_f] \times V(t) = [n_c(t) - n_f] \times V(t) \quad (13)$$

is an invariant quantity, i.e., $[k(t)/k(t_0)] = 1 \forall t$. If the net solute flux across the membrane is zero, then $n_f = n_0$ and the term $k(t) \times \alpha$ corresponds to the initial dry mass $m(t_0)$.

The above relation is used to illustrate the precision in the measurement of the RI of the transmembrane flux n_f . Figure 6(a) shows the calculated values of $k(t)/k(t_0)$ during an osmotic challenge averaged over $n = 8$ CHO cells in the field of view. The expression $k(t)/k(t_0)$ has been evaluated for different values of n_f . For a value of $n_f = 1.33456$, which

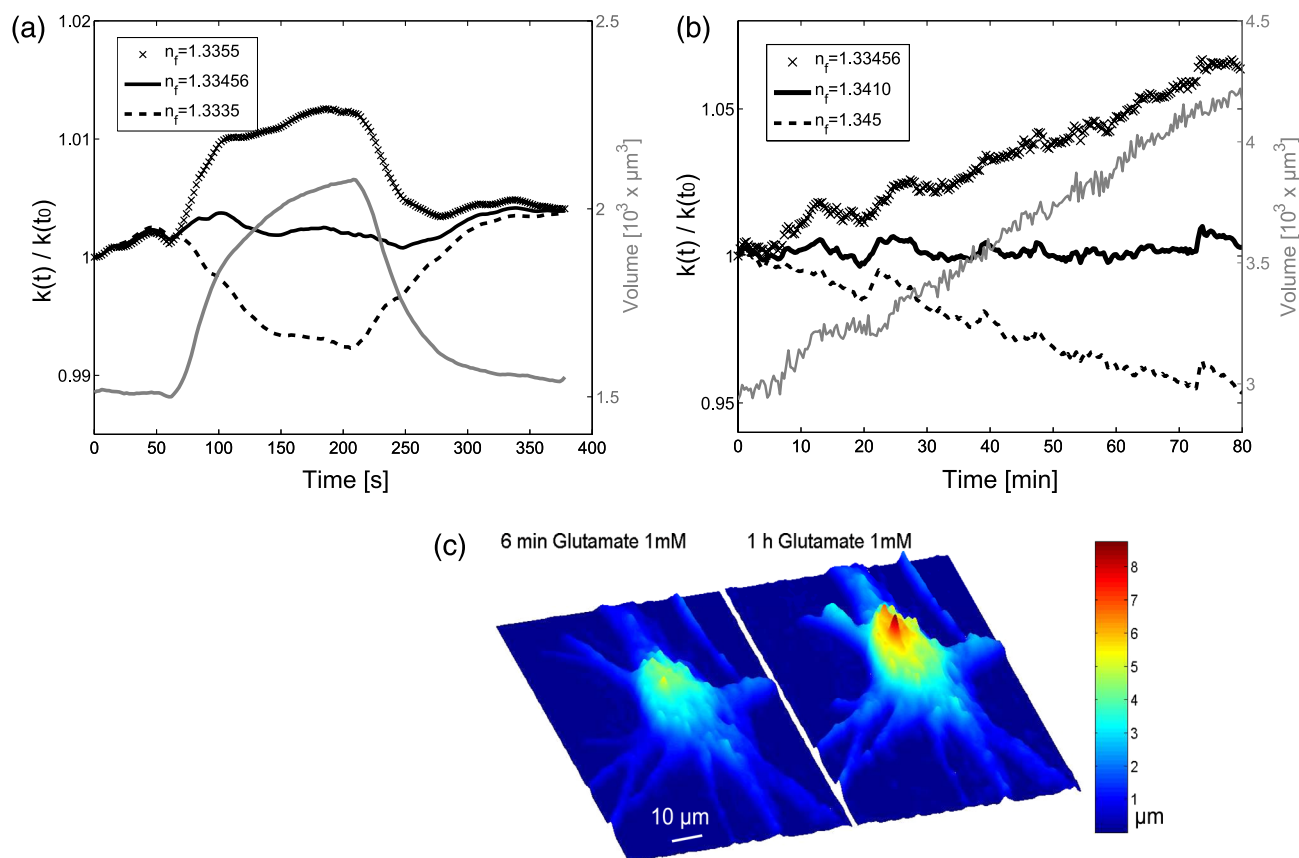


Fig. 6 Assessment of RI n_f of transmembrane flux. (a) Gray trace: mean volume time course of $n = 8$ CHO cells in field of view during the osmotic challenge. Black traces: the mean value $k(t)/k(t_0)$ of $n = 8$ CHO cells is evaluated for different values of n_f during a hypotonic challenge. For $n_f = n_{H_2O}$ the evaluated values $k(t)/k(t_0)$ are invariant throughout the experiment. (b) Gray trace: volume time course of an astrocyte when 1 mM glutamate is added to the extracellular solution. Glutamate was applied 6 min before hologram acquisition started and medium was not removed during the acquisition period. Cell swelling is observed throughout the acquisition period. Black traces: evaluated values $k(t)/k(t_0)$ for different values of n_f . For $n_f = 1.3410$ the evaluated values $k(t)/k(t_0)$ are invariant throughout the experiment. (c) Height profile image of astrocyte after 6 min and after 1 h of glutamate application.

corresponds to the RI of pure water at 543 nm wavelength (see Fig. 1), a ratio $k(t)/k(t_0)$ remarkably constant is obtained, i.e., presenting variations of only $\approx 0.4\%$ of the initial value. For values of $n_f = n_{H_2O} \pm 0.001$ the evaluated expression $k(t)/k(t_0)$ already varies by 1% during the osmotic challenge. This suggests that the osmotic induced transmembrane water flux is not accompanied by a net solute flux. Indeed, a different value of n_f can be expected if the water flux is accompanied by solute transport. To test this hypothesis, we applied glutamate to cultured astrocytes. Glutamate uptake into cultured astrocytes has been shown to induce cell swelling^{47–49} and the sodium coupled glutamate transporter is known to co-transport water together with glutamate and sodium.⁵⁰ Figure 6(b) shows the volume time course of an astrocyte bathing in a solution containing 1 mM glutamate. A steady volume increase is observed throughout the glutamate application period. The height profile image at the beginning and after 1 hr of glutamate exposure is shown in Fig. 6(c). The RI of transmembrane flux is evaluated by introducing the value n_f that leaves the measurement $k(t)/k(t_0)$ unaltered. A value of $n_f = 1.3401$ is determined [see Fig. 6(b)], clearly indicating that water and solutes are co-transported. For a value of $n_f = n_{H_2O}$ an increase of $\approx 6\%$ of the initial value $k(t_0)$ is observed after 80 min of glutamate exposure, indicating an accumulation of dry mass [in the sense of Eq. (9)] via glutamate uptake. Is a measured RI of transmembrane flux of 1.3410

possible? When considering a transmembrane flux of ≈ 300 mM of active solutes, which preserves intracellular osmolarity, one obtains a value of $\alpha_f \approx (n_f - n_{H_2O}/300 \text{ mM}) = 2.14 \times 10^{-5} \text{ mM}^{-1}$ for the specific refractive increment of the transmembrane flux. Based on the tables published in Ref. 51 refractive increments of α_f of 1.002×10^{-5} , 1.012×10^{-5} , and $3.16 \times 10^{-5} \text{ mM}^{-1}$ for KCl, NaCl and glucose solutions, respectively, are obtained. A value of α_f of $1.699 \times 10^{-5} \text{ mM}^{-1}$ for glutamate monosodium salt was derived from RI measurements with an Abbe-Refractometer, yielding an approximate value for α_f of 2.4×10^{-5} for a pure glutamate solution. Thus, the measured RI of transmembrane flux is in accordance with the refractive increments of the solutes involved in the transmembrane transport.

4.4 Influence of Dye on Cell Properties

Fast green FCF dye was chosen for this application for various reasons: first, it is an FDA approved food dye and presents relative low toxicity for living animals,⁵² second, it has a high molar extinction coefficient ($\epsilon_{625 \text{ nm}} = 102000 \text{ cm}^{-1} \text{ M}^{-1}$) which reduces the amount of dye that needs to be added to the extracellular solution to obtain a sufficient RI dispersion; and third, it presents a low diffusion rate across the cell membrane. Indeed no continuous drift of the measured signals due to

intracellular dye uptake could be detected for measurement periods longer than 1 h. However, synthetic food dyes are pharmacologically active substances and their use in nutrition is controversial.⁵³ For our application, the question must thus be addressed whether fast green FCF at high concentrations can influence cell properties? A study on hippocampal interneurons reported that fast green FCF reduced the frequency of synaptic events in a dose-dependent manner.⁵⁴ As amplitudes and kinetics of the miniature events were unaltered by fast green FCF, it was suggested that the dye acts primarily at a presynaptic locus. Likewise, our control experiments performed on cultured cortical neurons also revealed inhibitory effects of fast green FCF related to synaptic transmission. At the standard concentration of 20 mM fast green FCF, glutamate elicited transmembrane water movements²⁷ were strongly reduced. The phase shift ($\lambda = 682$ nm) upon application of glutamate (30 μ M, 30 s) was in average about 5- to 10-fold lower than in fast green-free solution. The effect was reversible. After washout of dye, typical phase responses to glutamate exposure were measured. Thus, the use of fast green FCF dye at a high concentration can limit the applicability of the method to study certain physiological processes like synaptic transmission in neurons. When studying specific transmembrane transport mechanisms, control experiments in dye free solution should therefore always be performed.

5 Conclusion

A method to measure absolute cell volume and intracellular RI in living cells is presented. The method, based on quantitative phase information reconstructed from a single hologram, is attractive because of its high temporal resolution, high measurement precision, and the full field of view acquisition scheme that requires no optical scanning. Here, we applied the method to quantitatively monitor osmotically induced cell volume changes and measure the membrane water permeability in different cell types. Further, we demonstrate how the method can provide information about the solutes accompanying water movements by accurately measuring the mean RI of transmembrane fluxes. The proposed method has a great potential in characterizing transmembrane transport processes and can contribute to a better understanding of water and ionic homeostasis at the single cell level. Furthermore, by providing quantitative measurements of absolute cell volume changes, membrane water permeability and mean RI of transmembrane fluxes the proposed method represents an efficient tool to explore the complex question of cell volume regulation.

Acknowledgments

We would like to thank Corinne Moratal and the collaborators of LyncéeTec for their technical assistance. This work was supported by the Swiss National Science Foundation, grant CR32I3-132993 to PM.

References

1. F. Lang et al., "Functional significance of cell volume regulatory mechanisms," *Physiol. Rev.* **78**(1), 247–306 (1998).
2. H. Pasantes-Morales and S. Cruz-Rangel, "Brain volume regulation: osmolytes and aquaporin perspectives," *Neuroscience* **168**(4), 871–884 (2010).
3. K. Strange, "Cellular volume homeostasis," *Adv. Physiol. Educ.* **28**(4), 155–159 (2004).
4. E. K. Hoffmann, I. H. Lambert, and S. F. Pedersen, "Physiology of cell volume regulation in vertebrates," *Physiol. Rev.* **89**(1), 193–277 (2009).
5. D. Bettega et al., "Cell thickness measurements by confocal fluorescence microscopy on c3h10t1/2 and v79 cells," *Int. J. Radiat. Biol.* **74**(3), 397–403 (1998).
6. N. J. Raat et al., "Measuring volume perturbation of proximal tubular cells in primary culture with three different techniques," *Am. J. Physiol.* **271**(1 Pt. 1), C235–C241 (1996).
7. M. A. Model, A. K. Khitritin, and J. L. Blank, "Measurement of the absorption of concentrated dyes and their use for quantitative imaging of surface topography," *J. Microsc.* **231**(1), 156–167 (2008).
8. J. L. Gregg et al., "Measurement of the thickness and volume of adherent cells using transmission-through-dye microscopy," *Pflugers Archiv-Eur. J. Physiol.* **460**(6), 1097–1104 (2010).
9. W. E. Crowe et al., "Volume changes in single n1e-115 neuroblastoma cells measured with a fluorescent probe," *Neuroscience* **69**(1), 283–296 (1995).
10. G. P. Nicchia et al., "Aquaporin-4-containing astrocytes sustain a temperature- and mercury-insensitive swelling *in vitro*," *Glia* **31**(1), 29–38 (2000).
11. E. Solenov et al., "Seven-fold reduced osmotic water permeability in primary astrocyte cultures from aquaporin-4 deficient mice measured by a calcein quenching method," *Am. J. Physiol.* **286**(2), C426–C432 (2003).
12. R. F. Kletzien et al., "A method using 3-O-methyl-D-glucose and phloretin for the determination of intracellular water space of cells in monolayer culture," *Anal. Biochem.* **68**(2), 537–544 (1975).
13. E. R. O'Connor et al., "Electrical resistance method for measuring volume changes in monolayer cultures applied to primary astrocyte cultures," *Am. J. Physiol.* **264**(2 Pt. 1), C471–C478 (1993).
14. J. Farinas and A. S. Verkman, "Cell volume and plasma membrane osmotic water permeability in epithelial cell layers measured by interferometry," *Biophys. J.* **71**(6), 3511–3522 (1996).
15. J. Klokkers et al., "Atrial natriuretic peptide and nitric oxide signaling antagonizes vasopressin-mediated water permeability in inner medullary collecting duct cells," *Am. J. Physiol. Renal Physiol.* **297**(3), F693–F703 (2009).
16. P. Marquet et al., "Digital holographic microscopy: a noninvasive contrast imaging technique allowing quantitative visualization of living cells with subwavelength axial accuracy," *Opt. Lett.* **30**(5), 468–470 (2005).
17. G. Popescu et al., "Diffraction phase microscopy for quantifying cell structure and dynamics," *Opt. Lett.* **31**(6), 775–777 (2006).
18. F. Dubois et al., "Digital holographic microscopy for the three-dimensional dynamic analysis of *in vitro* cancer cell migration," *J. Biomed. Opt.* **11**(5), 054032 (2006).
19. I. Moon and B. Javidi, "Three-dimensional identification of stem cells by computational holographic imaging," *J. R. Soc. Interface* **4**(13), 305–313 (2007).
20. D. Carl et al., "Parameter-optimized digital holographic microscope for high-resolution living-cell analysis," *Appl. Opt.* **43**(36), 6536–6544 (2004).
21. B. Rappaz et al., "Measurement of the integral refractive index and dynamic cell morphometry of living cells with digital holographic microscopy," *Opt. Express* **13**(23), 9361–9373 (2005).
22. N. Lue et al., "Live cell refractometry using microfluidic devices," *Opt. Lett.* **31**(18), 2759–2761 (2006).
23. B. Kemper et al., "Integral refractive index determination of living suspension cells by multifocus digital holographic phase contrast microscopy," *J. Biomed. Opt.* **12**(5), 054009 (2007).
24. B. Rappaz et al., "Simultaneous cell morphometry and refractive index measurement with dual-wavelength digital holographic microscopy and dye-enhanced dispersion of perfusion medium," *Opt. Lett.* **33**(7), 744–746 (2008).
25. J. Kühn et al., "Real-time dual-wavelength digital holographic microscopy with a single hologram acquisition," *Opt. Express* **15**(12), 7231–7242 (2007).
26. M. Belanger et al., "Role of the glyoxalase system in astrocyte-mediated neuroprotection," *J. Neurosci.* **31**(50), 18338–18352 (2011).
27. P. Jourdain et al., "Determination of transmembrane water fluxes in neurons elicited by glutamate ionotropic receptors and by the cotransporters kcc2 and nkcc1: a digital holographic microscopy study," *J. Neurosci.* **31**(33), 11846–11854 (2011).

28. M. Daimon and A. Masumura, "Measurement of the refractive index of distilled water from the near-infrared region to the ultraviolet region," *Appl. Opt.* **46**(18), 3811–3820 (2007).
29. E. Cuche, P. Marquet, and C. Depeursinge, "Simultaneous amplitude-contrast and quantitative phase-contrast microscopy by numerical reconstruction of fresnel off-axis holograms," *Appl. Opt.* **38**(34), 6994–7001 (1999).
30. R. Barer, "Interference microscopy and mass determination," *Nature* **169**(4296), 366–367 (1952).
31. R. Barer and D. A. Dick, "Interferometry and refractometry of cells in tissue culture," *Exp. Cell Res.* **13**(Suppl. 4), 103–35 (1957).
32. G. E. Perlmann and L. G. Longworth, "The specific refractive increment of some purified proteins," *J. Am. Chem. Soc.* **70**(8), 2719–2724 (1948).
33. A. S. Verkman, "Water permeability measurement in living cells and complex tissues," *J. Membr. Biol.* **173**(2), 73–87 (2000).
34. N. Mohandas and E. Evans, "Mechanical-properties of the red-cell membrane in relation to molecular-structure and genetic-defects," *Annu. Rev. Biophys. Biomol. Struct.* **23**, 787–818 (1994).
35. M. L. Zeidel et al., "Ultrastructure, pharmacologic inhibition, and transport selectivity of aquaporin chip in proteoliposomes," *Biochem.* **33**(6), 1606–1615 (1994).
36. J. Voigtlaender, B. Heindl, and B. F. Becker, "Transmembrane water influx via aquaporin-1 is inhibited by barbiturates and propofol in red blood cells," *Naunyn-Schmiedeberg's Arch. Pharmacol.* **366**(3), 209–217 (2002).
37. J. Farinas et al., "Plasma membrane water permeability of cultured cells and epithelia measured by light microscopy with spatial filtering," *J. Gen. Physiol.* **110**(3), 283–296 (1997).
38. J. Gao et al., "Acetazolamide inhibits osmotic water permeability by interaction with aquaporin-1," *Anal. Biochem.* **350**(2), 165–170 (2006).
39. E. Gunnarson et al., "Identification of a molecular target for glutamate regulation of astrocyte water permeability," *Glia* **56**(6), 587–596 (2008).
40. M. Amiry-Moghaddam, E. H. Hoddevik, and O. P. Ottersen, "Aquaporins: multifarious roles in brain," *Neuroscience* **168**(4), 859–861 (2010).
41. A. Yool, "Aquaporins: multiple roles in the central nervous system," *The Neuroscientist* **13**(5), 470–485 (2007).
42. J. Badaut et al., "Aquaporins in brain: distribution, physiology, and pathophysiology," *J. Cereb. Blood Flow Metab.* **22**(4), 367–378 (2002).
43. N. MacAulay et al., "Passive water and urea permeability of a human Na⁺-glutamate cotransporter expressed in xenopus oocytes," *J. Physiol.* **542**(3), 817–828 (2002).
44. P. G. Aitken et al., "Volume changes induced by osmotic stress in freshly isolated rat hippocampal neurons," *Pflugers Archiv-Eur. J. Physiol.* **436**(6), 991–998 (1998).
45. R. D. Andrew et al., "Physiological evidence that pyramidal neurons lack functional water channels," *Cereb. Cortex* **17**(4), 787–802 (2007).
46. H. Zhao, P. H. Brown, and P. Schuck, "On the distribution of protein refractive index increments," *Biophys. J.* **100**(9), 2309–2317 (2011).
47. A. S. Bender et al., "Ionic mechanisms in glutamate-induced astrocyte swelling: Role of k^+ influx," *J. Neurosci. Res.* **52**(3), 307–321 (1998).
48. G. H. Schneider, A. Baethmann, and O. Kempfski, "Mechanisms of glial swelling induced by glutamate," *Can. J. Physiol. Pharmacol.* **70**(S1), S334–S343 (1992).
49. Y. Koyama et al., "A morphological study on glutamate-induced swelling of cultured astrocytes: involvement of calcium and chloride ion mechanisms," *Neurosci. Lett.* **124**(2), 235–238 (1991).
50. N. MacAulay et al., "Water transport by the human Na⁺-coupled glutamate cotransporter expressed in xenopus oocytes," *J. Physiol.* **530**(3), 367–378 (2001).
51. D. R. Lide et al., *CRC Handbook of Chemistry and Physics*, 87th ed., pp. 52–77, CRC Press, Boca Raton, Florida (2006).
52. W. H. Hansen et al., "Chronic toxicity of three food colourings: guinea green b, light green sf yellowish and fast green FCF in rats, dogs and mice," *Food Cosmet. Toxicol.* **4**(4), 389–410 (1966).
53. S. Kobylewski and M. F. Jacobson, "Toxicology of food dyes," *Int. J. Occup. Environ. Health* **18**(3), 220–246 (2012).
54. J. A. van Hooft, "Fast green FCF (food green 3) inhibits synaptic activity in rat hippocampal interneurons," *Neurosci. Lett.* **318**(3), 163–165 (2002).